This is a repository copy of *Recent improvements in quantification of energy-dispersive X-ray spectra and maps in electron microscopy of semiconductors*.

White Rose Research Online URL for this paper:
https://eprints.whiterose.ac.uk/215066/

Version: Published Version

Article:

Walther, T. orcid.org/0000-0003-3571-6263 (2024) Recent improvements in quantification of energy-dispersive X-ray spectra and maps in electron microscopy of semiconductors. Applied Research, 3 (6). e202300128. ISSN 2702-4288

https://doi.org/10.1002/appl.202300128

Reuse
This article is distributed under the terms of the Creative Commons Attribution (CC BY) licence. This licence allows you to distribute, remix, tweak, and build upon the work, even commercially, as long as you credit the authors for the original work. More information and the full terms of the licence here: https://creativecommons.org/licenses/

Takedown
If you consider content in White Rose Research Online to be in breach of UK law, please notify us by emailing eprints@whiterose.ac.uk including the URL of the record and the reason for the withdrawal request.

eprints@whiterose.ac.uk
https://eprints.whiterose.ac.uk/

Check for updates

Received: 30 November 2023 | Revised: 8 July 2024 | Accepted: 18 July 2024

DOI: 10.1002/appl.202300128

Applied Research

RESEARCH ARTICLE

Recent improvements in quantification of energy-dispersive X-ray spectra and maps in electron microscopy of semiconductors

Thomas Walther

Department of Electronic and Electrical Engineering, University of Sheffield, Sheffield, UK

Correspondence
Thomas Walther, Department of Electronic and Electrical Engineering, University of Sheffield, Sheffield S1 3JD, UK.
Email: t.walther@sheffield.ac.uk

Abstract

This tutorial-style article describes recent improvements in the quantitative application of energy-dispersive X-ray spectroscopy and mapping in electron microscopes to semiconductors, with a focus on spatial resolution, sensitivity and accuracy obtainable in characterising the chemical composition of thin layers, quantum wells and quantum dots. Various approaches applicable in scanning electron microscopy of bulk and (scanning) transmission electron microscopy of thin film samples are outlined. Applications to semiconductor quantum well systems, mainly based on indium gallium arsenide and silicon germanium studied in the author's laboratory, are provided as examples.

KEYWORDS

InGaAs, quantum dots, quantum wells, SEM, SiGe, TEM, X-ray spectroscopy

INTRODUCTION

Energy-dispersive X-ray spectroscopy (EDXS) is an analytical method to measure the chemical composition of a material. The method records and interprets the characteristic X-rays emitted from an electron-irradiated sample, either in a scanning electron microscope (SEM) or in a (scanning) transmission electron microscope (STEM/TEM). These characteristic X-rays are the result from inelastic electron scattering in the sample, successive ionisation of some atoms and the eventual relaxation of outer-shell bound electrons when they relax into the free states freed up in lower shells of those ionised atoms. The latter de-excitation can occur either radiatively, producing characteristic X-rays, or nonradiatively, producing Auger electrons, both of which are element-specific signals. There are some excellent textbooks that describe the physics of X-ray generation, detection and analysis in SEM [1, 2] or (S)TEM [3], where the main difference is that SEM usually studies bulk samples that produce a lot of X-rays but from a fairly large excitation volume, hence gives strong signals with micron-scale spatial resolution, while (S)TEM utilises much thinner, electron transparent samples that produce far fewer X-rays but from a much smaller region, providing noisy signals at nanoscale and sometimes even near-atomic spatial resolution that is more difficult to quantify in terms of compositional accuracy.

The aim of this article is to demonstrate by way of examples that there are ways to get X-ray maps from atomically thin layers in even basic SEM-EDXS instruments and to measure the chemical composition of thin layers or quantum dots in STEM with at% accuracy at a few nanometres resolution. Also, we describe our k^*-factor method [4–6] for self-consistent absorption correction in (S)TEM-EDX, discuss its merits and drawbacks and present some applications to InGaAs and SiGe alloys.

This is an open access article under the terms of the Creative Commons Attribution License, which permits use, distribution and reproduction in any medium, provided the original work is properly cited.
© 2024 The Author(s). *Applied Research* published by Wiley-VCH GmbH.

METHODS

Simulations

Key to quantifying X-ray spectra is the ability to simulate the electron–matter interaction by Monte Carlo simulations and to estimate X-ray absorption within the sample, the detector window and the dead layer formed beneath the top electrode contact onto the reverse-biased diode that makes up the solid-state detector (most often, silicon), in particular at low energies where many soft X-rays can be absorbed [7].

Here, we use the CASINO v2.42 programme [8] to model the electron interaction with the sample, X-ray generation and detection using a Si:Li solid state detector with 300 nm polymer window. The now widely available silicon drift detectors (SSDs) can be operated windowless because they need less cooling and so are not susceptible to condensation and contamination under poor vacuum conditions, improving soft X-ray detection, but as they are much thinner (wafer thicknesses are typically 350–500 µm) they are less sensitive to harder X-rays, some of which will traverse them without being detected.

In an SEM, bulk samples are investigated that can be easily prepared. Spatial resolution is often poor because the electron beam can penetrate deep into the sample, and due to multiple elastic–inelastic scattering the interaction volume will be large [7]. Typical lateral widths of this interaction volume are in the range of 100 nm–1 µm. The spatial resolution can only be improved in three ways:

(i) reducing the electron beam voltage to reduce the overall interaction volume (which however will also reduce the number of X-rays produced as well as restrict the line types that can be studied, due to the Duane–Hunt limit, cf. Figure 1 below [9]),
(ii) analysing the near-surface regions where the interaction volume is still relatively small (near the stalk or stem of the pear-shaped interaction volume in Figure 2), which allows high-resolution mapping of surface features, such as quantum dots on a wafer surface [9] or measuring the thickness of single thin films on surfaces [10].
(iii) reducing the sample thickness to cut off the largest part of the interaction volume in the bulk, effectively employing thin TEM samples in SEM [11]. In bulk samples, multiple electron scattering spreads the probe so much that signals from cross-sectioned layers thinner than the probe size become very weak, as in Figure 3.

Bulk samples contain the complete interaction volume of all electrons that have lost all their energy until they are absorbed by or reflected from the specimen, all of which can be comprehensively modelled by Monte Carlo methods down to a minimum cut-off

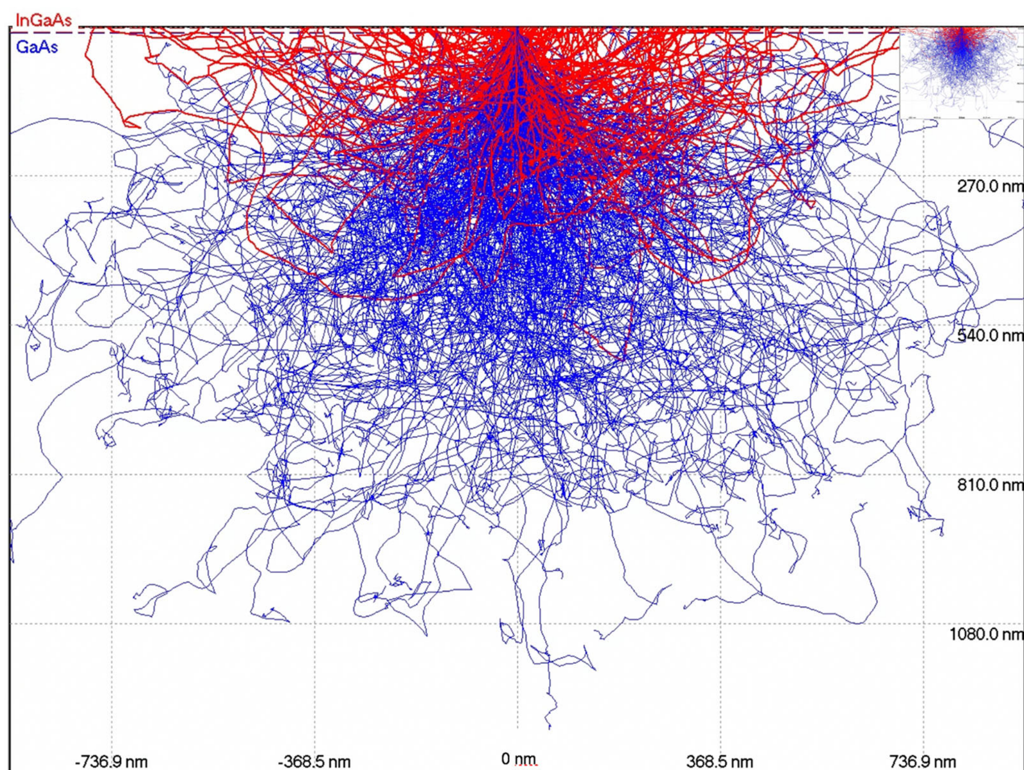

FIGURE 1 Monte Carlo simulation of electron interaction with 10 nm InGaAs on GaAs. 5 nm electron beam at 4 kV (insert at top right) and 15 kV. The latter is 8× larger. Red (displayed in the foreground): backscattered, blue (background): absorbed electrons. *Source*: Adapted from Walther [9].

27024288, 0, Downloaded from https://onlinelibrary.wiley.com/doi/10.1002/appl.202300128 by University Of Sheffield, Wiley Online Library on [06/08/2024]. See the Terms and Conditions (https://onlinelibrary.wiley.com/terms-and-conditions) on Wiley Online Library for rules of use; OA articles are governed by the applicable Creative Commons License

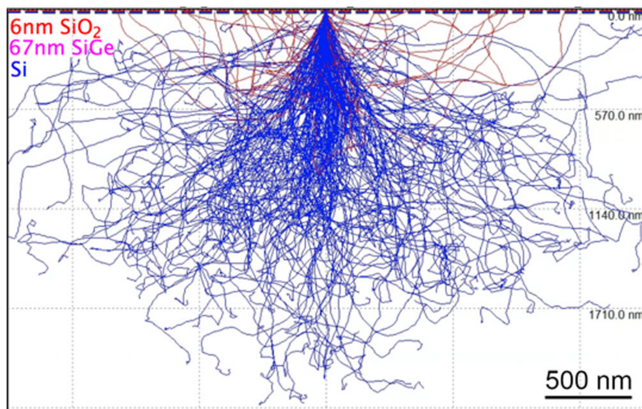

FIGURE 2 Monte Carlo simulation of electron interaction with 6 nm SiO_2 on 67 nm SiGe/Si at 15 kV. Red (displayed in the background): backscattered, blue (displayed in the foreground): absorbed electrons. *Source*: Adapted from Walther [10].

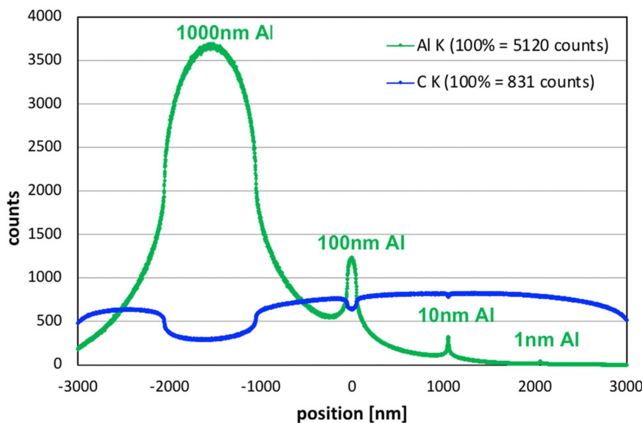

FIGURE 3 Monte Carlo simulation of thin Al layers in graphite imaged edge-on (bulk, 15 kV, 30 nm probe size, intensities from bulk references as indicated in brackets).

energy (set by default as 50 eV in CASINO). Programmes such as ZAF, PROZA, PAP, XPP and other Φ(ρz) approaches [12] can model X-ray generation, emission and absorption slice by slice, including secondary fluorescence [13], and so quantify X-ray intensities, the biggest remaining error usually being the detector efficiency for soft X-rays.

In a TEM or STEM, electron transparent thin foil samples are investigated, which reduces the interaction volume significantly and thereby improves the spatial resolution, but the number of X-rays produced is thereby reduced also, and large solid-state X-ray detectors can often not be brought close enough to the point where the electron beam hits the sample because the latter sits within a narrow, cone-shaped pole-piece of the objective lens. Hence, count numbers are often low and maps quite noisy. There are again a number of important points:

(a) While there have been examples of atomic lattice-resolved X-ray maps at 0.4 [14] and 0.8 nm [15] resolution, the pseudo-coloured maps presented do not actually state contrast levels, and line scans across similar structures often turn out to be far too noisy to assess spatial resolution properly. Usually, atomic resolution will only be possible at certain foil thicknesses and directions, and multislice simulations will be needed to assure which atomic columns the X-ray signals actually come from Forbes et al. [16] before any interpretation beyond qualitative chemical distribution can be made.

(b) Lattice resolution is only possible along zone-axis orientations which, similar to two-beam conditions, should generally be avoided for quantification because of possible channelling effects.

(c) Maps from thin foil samples are not easily interpretable in terms of atomic concentrations because of surface effects (1 nm oxide layers on top and below a 40 nm thin sample can change results by 5%) and local thickness variations (so only ratios of intensities will be meaningful but will be even noisier than raw maps [17]).

Compositional precision relates to self-consistency of individual as well as the reproducibility of consecutive measurements, both of which are often poor. For stoichiometric alloys like GaAs, for example, the Ga/As elemental ratio reported may be far off unity but will depend on which lines are chosen, cf. Figure 10 [18]. Most acquisition software packages decide automatically which X-ray lines they use for quantification (usually the hardest X-ray lines available, that is, K lines preferred over L or M); however, choosing other lines manually can give significantly different results in case of both SEM-EDXS and (S)TEM-EDXS. While this may appear confusing, it allows for self-consistency checks that can improve reliable quantification in (S)TEM-EDXS of many semiconductors, by serving as internal self-calibration of absorption effects. The number of X-rays detected from an element j in a sample of thickness t is given by

$$I_j = N_A i \rho t c_j \sigma_j \omega_j f_j e_j \tau a_j / (A_j e),$$

where N_A is Avogadro's constant, i the probe current, ρ the sample density, c_j the weight fraction, σ_j the ionisation cross-section, ω_j the fluorescence yield, f_j the line partitioning fraction (for K, L, M lines), e_j the detection efficiency of line j, τ the measurement time, a_j the absorption correction factor, A_j the atomic weight of element j (in g/mol) and e the electron charge [6]. In this expression, secondary fluorescence between X-rays is neglected but could be incorporated phenomenologically into the absorption correction factor. In (S)TEM, the specimen is a thin foil, so the excitation volume is small and the spatial resolution can reach sub-nm, but the signal is noisy and quantification relies on a correct absorption correction. There are only five options:

(i) thin film approximation after Cliff & Lorimer without absorption correction [19], where for any line pair i,j k-factors are defined as $k_{i,j} = (\sigma_j\ \omega_j\ f_j\ e_j\ A_i)/(\sigma_i\ \omega_i\ f_i\ e_i\ A_j)$. The central question is when a specimen will be thin enough to neglect absorption, and what the error will be. Tixier and Philibert [20] defined as criterion for

27024288, 0, Downloaded from https://onlinelibrary.wiley.com/doi/10.1002/appl.202300128 by University Of Sheffield, Wiley Online Library on [06/08/2024]. See the Terms and Conditions (https://onlinelibrary.wiley.com/terms-and-conditions) on Wiley Online Library for rules of use; OA articles are governed by the applicable Creative Commons License

neglecting an absorption correction that the product of mass attenuation coefficient μ/ρ, cosecant of the take-off angle β, density ρ and sample thickness Δz be <0.1. The absorption correction factor at a depth z for take-off angle β would be exp $-[(\mu/\rho)\ \mathrm{cosec}\beta\ \rho z]$, so after integration of absorption over the foil thickness from the top at $z = 0$ to the bottom at $z = \Delta z$, exp $-[\frac{1}{2}(\mu/\rho)\ \mathrm{cosec}\beta\ \rho\ \Delta z] = \exp - 0.05 \approx 0.95$, that is, the absorption would change quantification of each X-ray line by 5% relative with this criterion. Watanabe and Williams [21] also chose the 5% absorption correction threshold and showed that for pure elements this converted into ≤30 nm specimen thickness for K-lines and ≤20 nm specimen thickness for L-lines. If one needed more accurate absorption correction, then still thinner specimens would be needed for calibration; however, the influence of surface contamination and in particular surface oxides would become paramount for semiconductors and metals.

(ii) measurement of the thickness and modelling of absorption assuming a certain density, then division of the k-factor for thin films by a built-in absorption correction factor $a \in (0,1]$ to compensate for the absorption (most common software approach). For the calculation of absorption, the sample geometry must be known. In commercial software, only samples of 'parallel slab' geometry are assumed, for which a_j can be computed using an analytical expression. For nanorods or other shapes, absorption factors cannot be calculated without numerical integration or simulation.

(iii) performing quantification with or without absorption correction as a function of specimen thickness, followed by backwards extrapolation to zero thickness [22]. The biggest drawback of this is that one needs a series of spectra from different thicknesses and so will get, at best, only the composition under the assumption that the material was homogenous.

(iv) measurement of the probe current and use of the ζ-factor method which has been tested particularly for metal alloys and oxides and may be the best choice for specimens consisting of light elements only [21, 23].

(v) quantification using the effective k^* factor method where $k_{ij}^* = k_{ij}\, a_j/a_i$ is the ratio of the thin film k-factor and the corresponding absorption correction factors and should be plotted *not* as a function of real thickness (which is difficult to measure) but the K/L or L/M line ratio of one heavier element that can be extracted from the same spectrum [4, 23]. This necessitates having at least one heavy element with $Z > 20$ in the specimen whose K/L ratio (or L/M) can be used for internal reference. For alloys where the concentration of the reference element is constant (e.g. as in InGaAs makes up 50 at %), one gets a single calibration curve showing how the thin film absorption factor for minimal K/L ratio changes as K/L increases with increasing thickness, c.f. Figure 4a,c [6]. If the concentration of

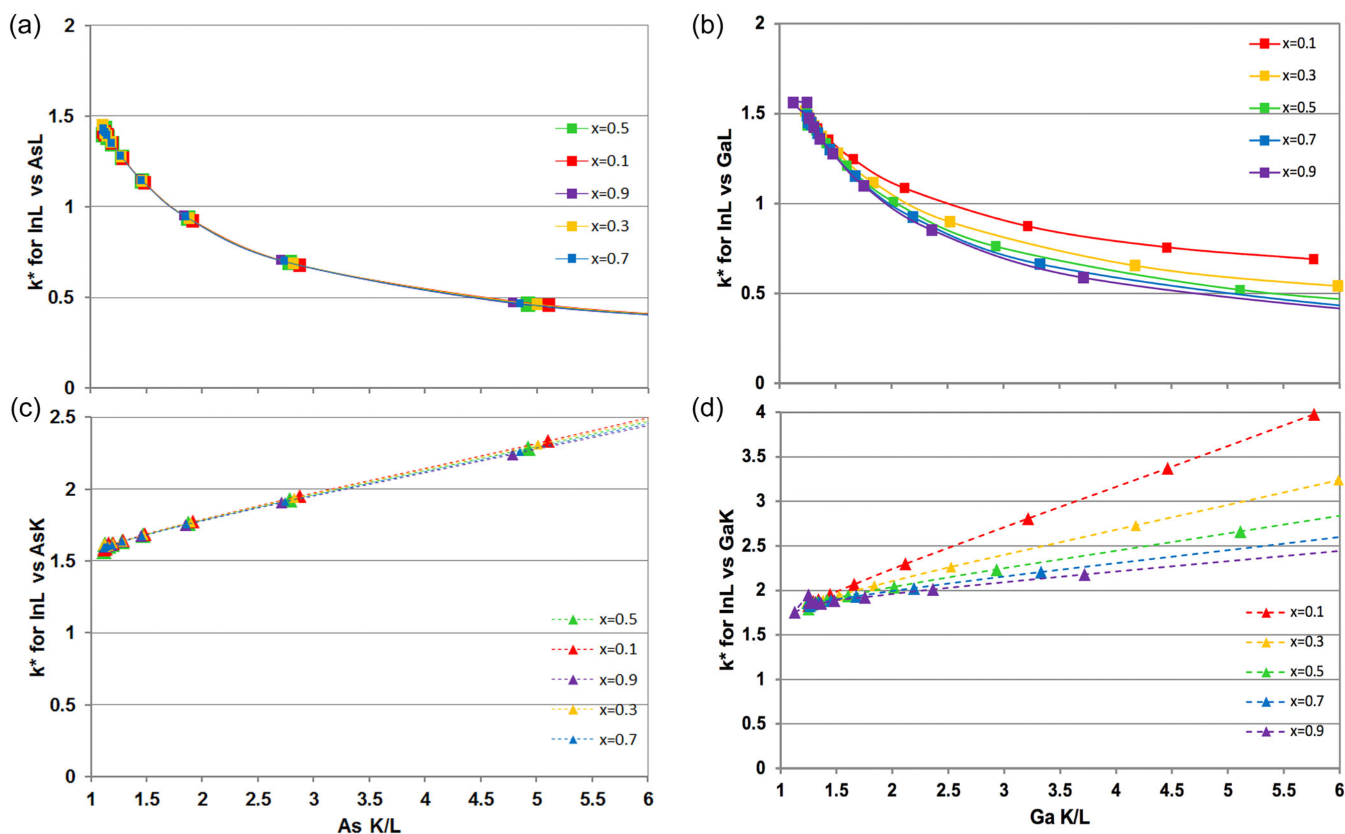

FIGURE 4 Monte Carlo simulation of variation of k^*-factors of In L-line with respect to As L-line (a), Ga L-line (b), As K-line (c) or Ga K-line (d) with thickness for $In_xGa_{1-x}As$ alloys for different indium content, x [6, 24].

27024288, 0, Downloaded from https://onlinelibrary.wiley.com/doi/10.1002/appl.202300128 by University Of Sheffield, Wiley Online Library on [06/08/2024]. See the Terms and Conditions (https://onlinelibrary.wiley.com/terms-and-conditions) on Wiley Online Library for rules of use; OA articles are governed by the applicable Creative Commons License

the reference element is not constant when the one whose content is to be measured is varied (e.g. Ga in InGaN, or Ge in SiGe) one will get sets of calibration curves for different densities that necessitate an iterative solution, c.f. Figure 4b,d [24]. Some applications to InGaAs and SiGe are presented in Section 3.2.

Electron microscopy

For the electron microscopy, several different instruments have been used, that is,

- for SEM-EDX: a Hitachi TM3030 + SEM with W hairpin filament, operated at 15 kV and equipped with a 30 mm^2 Bruker SDD with ultrathin window;
- for STEM-EDX: a Zeiss Libra 200FE with Cs-corrector and a JEOL 2010F, both with Schottky field-emission gun (FEG) and Oxford Instruments Si:Li detector with 0.13 srad collection angle, or a JEOL F200 with cold FEG and JEOL double-SDDs with a total collection angle of 1.7 srad. All (S)TEMs have been operated at 200 kV.

Materials and sample preparation

The InGaAs thin films and quantum well systems used for this study were all grown by molecular-beam epitaxy. Those for SEM studies consisted of single InAs or single $In_{0.2}Ga_{0.8}As$ layers deposited on GaAs(001) substrates. The $Si_{0.54}Ge_{0.46}$ bulk sample was grown at Tohoku University by the Czochralski method. SiGe thin films of various germanium concentrations were grown at the University of Warwick by chemical vapour deposition. All samples for transmission electron microscopy were prepared by standard methods of cutting, mechanical grinding, polishing by 3 and 1 µm diamond paste and subsequent argon ion milling at initially 4 kV and finally 2 kV until electron transparency.

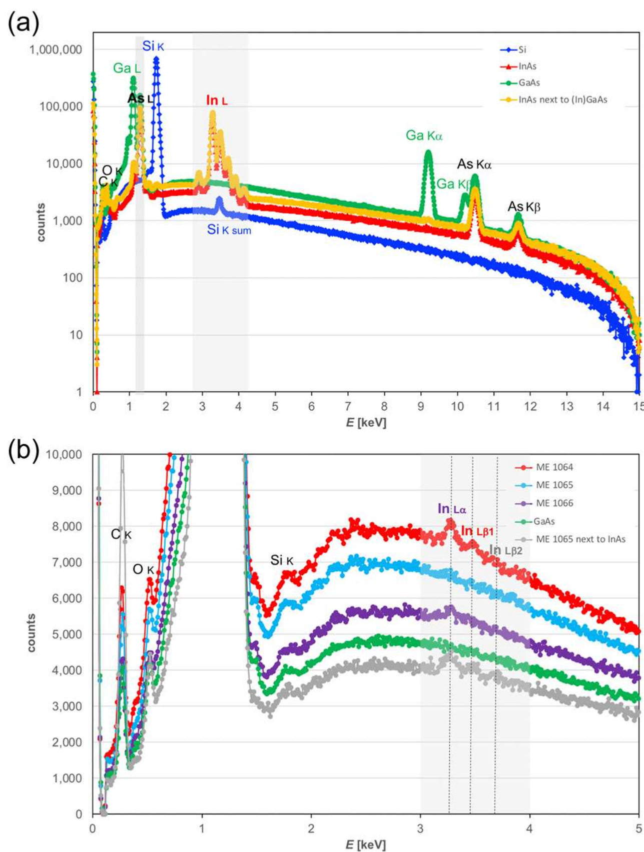

FIGURE 5 X-ray spectra at 15 kV from the surfaces of Si, InAs and GaAs wafers as well as the same InAs wafer adjacent to a piece of (In)GaAs wafer (a) and from GaAs wafers with different InGaAs layers on top (nominally 10, 5 and 2 nm of $In_{0.2}Ga_{0.8}As$ for ME1064, 1065 and 1066, respectively) as well as InGaAs next to a piece of InAs wafer (b). The orange and grey spectra show that Ga K stray signals are very low while In L stray signals could be high and contribute an unwanted background. The Si K signal comes from the silicon drift detector itself. *Source*: Adapted from Walther [9].

RESULTS

SEM-EDX

Figures 5 and 6 below demonstrate that in a sub-nm InGaAs thin film at the onset of the Stranski–Krastanow growth, In-rich undulations and islands form that are under 100 nm in width and a few nanometres in height and can not only be clearly imaged but can as well be mapped in EDX mode. Using experimental spectra of InAs, GaAs and Si in Figure 5a) as references to calibrate the In/As X-ray yield, the detection limit for indium was evaluated from various layers of single InGaAs thin films on GaAs as shown in Figure 5b) and found from the standard deviation of the In_L/As_L ratio as 0.7 ± 0.1 ML (InAs

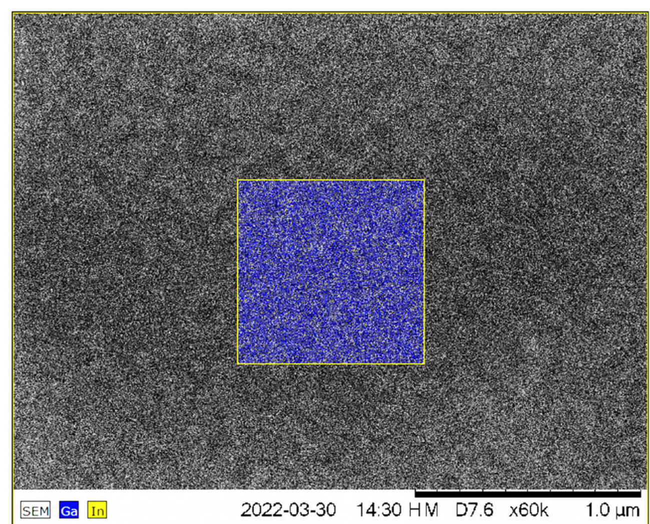

FIGURE 6 Secondary electron image with coloured X-ray map of central (0.8 µm)^2 region of a thin pure InAs layer on surface of GaAs at 15 kV (nom. thickness: 0.45 nm, exp. value calculated: 0.81 ± 0.24 nm) [9].

27024288, 0, Downloaded from https://onlinelibrary.wiley.com/doi/10.1002/appl.202300128 by University Of Sheffield, Wiley Online Library on [06/08/2024]. See the Terms and Conditions (https://onlinelibrary.wiley.com/terms-and-conditions) on Wiley Online Library for rules of use; OA articles are governed by the applicable Creative Commons License

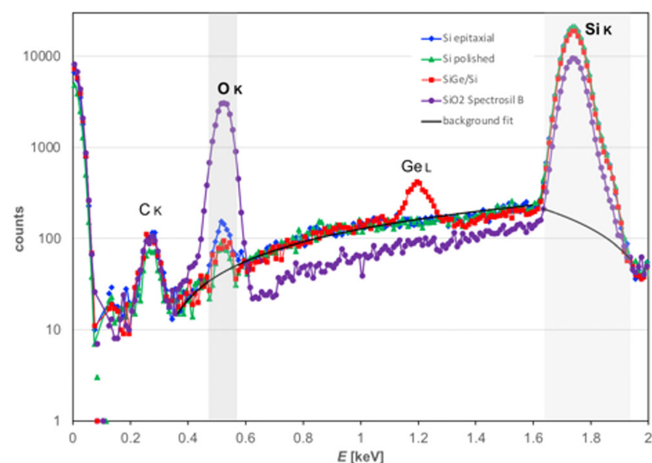

FIGURE 7 X-ray spectra from different surface oxides of Si, SiGe and SiO_2. *Source*: Adapted from Walther [10].

equivalent monolayers) as long as neither InAs nor Si wafer parts were in the vicinity of the analysis (as both would give spurious indium signals due to either fluorescence or silicon sum peaks).

Despite the noise, surface corrugations on the lateral scale of about 100–200 nm can be seen in Figure 6, and the average indium amount can be measured from comparison of the integrated X-ray spectrum to those X-ray spectra from InGaAs layers in Figure 5.

Figure 7 shows that the X-ray spectra from Si and SiGe wafers reveal different oxygen signals the thickness of which can be determined if measured relative to an SiO_2 Spectrosil B sample and compared with simulations. Here, the oxide layer on the SiGe wafer had an inferred thickness of 6.1 ± 0.7 nm which was in excellent agreement with a direct measurement by bright-field TEM of 6.5 ± 0.3 nm. The thinnest native surface oxide thickness on a recently polished Si wafer could be determined in top-down geometry as 1.7 ± 0.3 nm (green line in Figure 7), but the detection limit would generally lie around 1 nm due to a weak

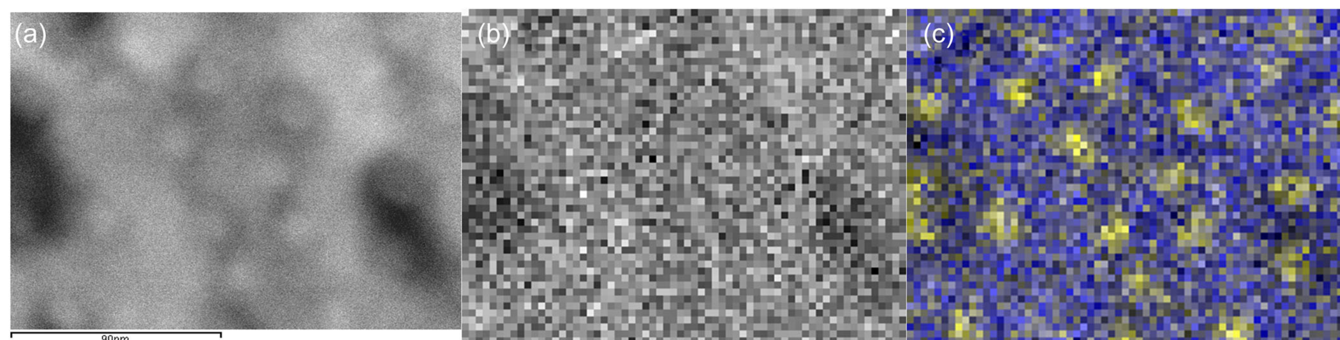

FIGURE 8 200 kV ADF STEM image (a) of capped InGaAs quantum dots in top view and X-ray maps of As K (b), In L and Ga K as composite map (c), showing lack of overgrowth around islands despite capping by nominally 8 nm GaAs. Sampling: 3 nm/pixel. *Source*: Adapted from Liew et al. [25]. ADF, annular dark-field; STEM, scanning transmission electron microscope.

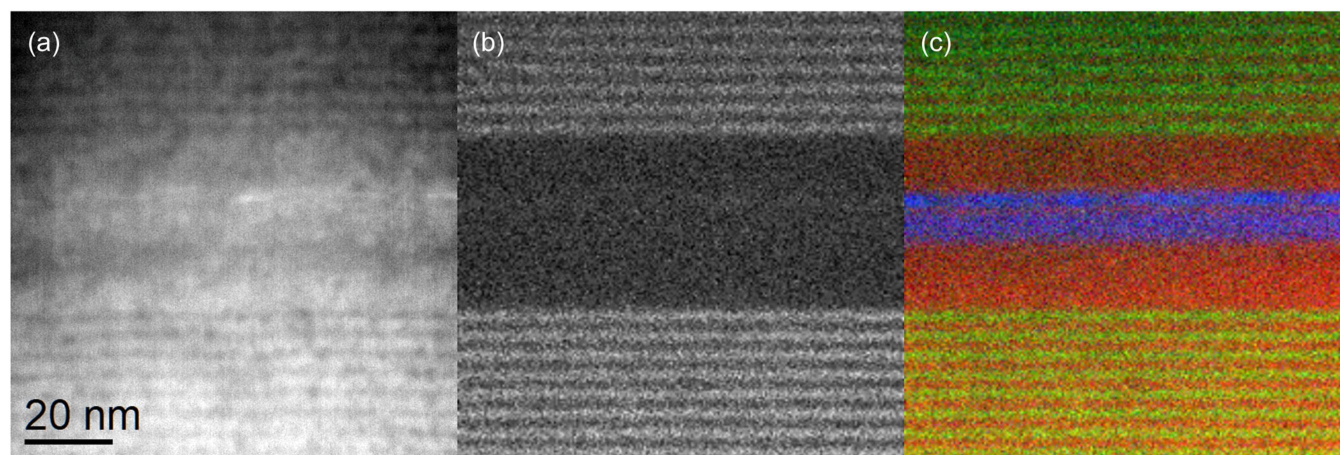

FIGURE 9 200 kV ADF STEM image of In(Al)GaAs quantum wells in cross-section (a), X-ray map of Al K signal (b); map of Ga K, Al K, In L intensities, as composite RGB map (c). The weak Al signal within the upper InGaAs layer corresponds to 0.3 monolayers (<0.1 nm) [27]. ADF, annular dark-field; RGB, red, blue, green; STEM, scanning transmission electron microscope.

27024288, 0, Downloaded from https://onlinelibrary.wiley.com/doi/10.1002/appl.202300128 by University Of Sheffield, Wiley Online Library on [06/08/2024]. See the Terms and Conditions (https://onlinelibrary.wiley.com/terms-and-conditions) on Wiley Online Library for rules of use; OA articles are governed by the applicable Creative Commons License

remaining O signal found in all X-ray spectra, which could be due to either the polymer entrance window of the detector used or surface contamination from the cleaning solvents. While this highlights the challenges compared to ultrahigh vacuum surface analysis techniques where samples could be out-gassed in situ, the result nevertheless demonstrates the power of simple SEM-EDXS in top-down geometry.

(S)TEM-EDX

Figure 8 depicts the superior lateral resolution of 200 kV STEM-EDX when performing X-ray mapping in top-down geometry of 10 nm diameter InGaAs quantum dots deposited on a GaAs wafer. Spatial resolution is around 1–2 nm and sufficient to show not only the

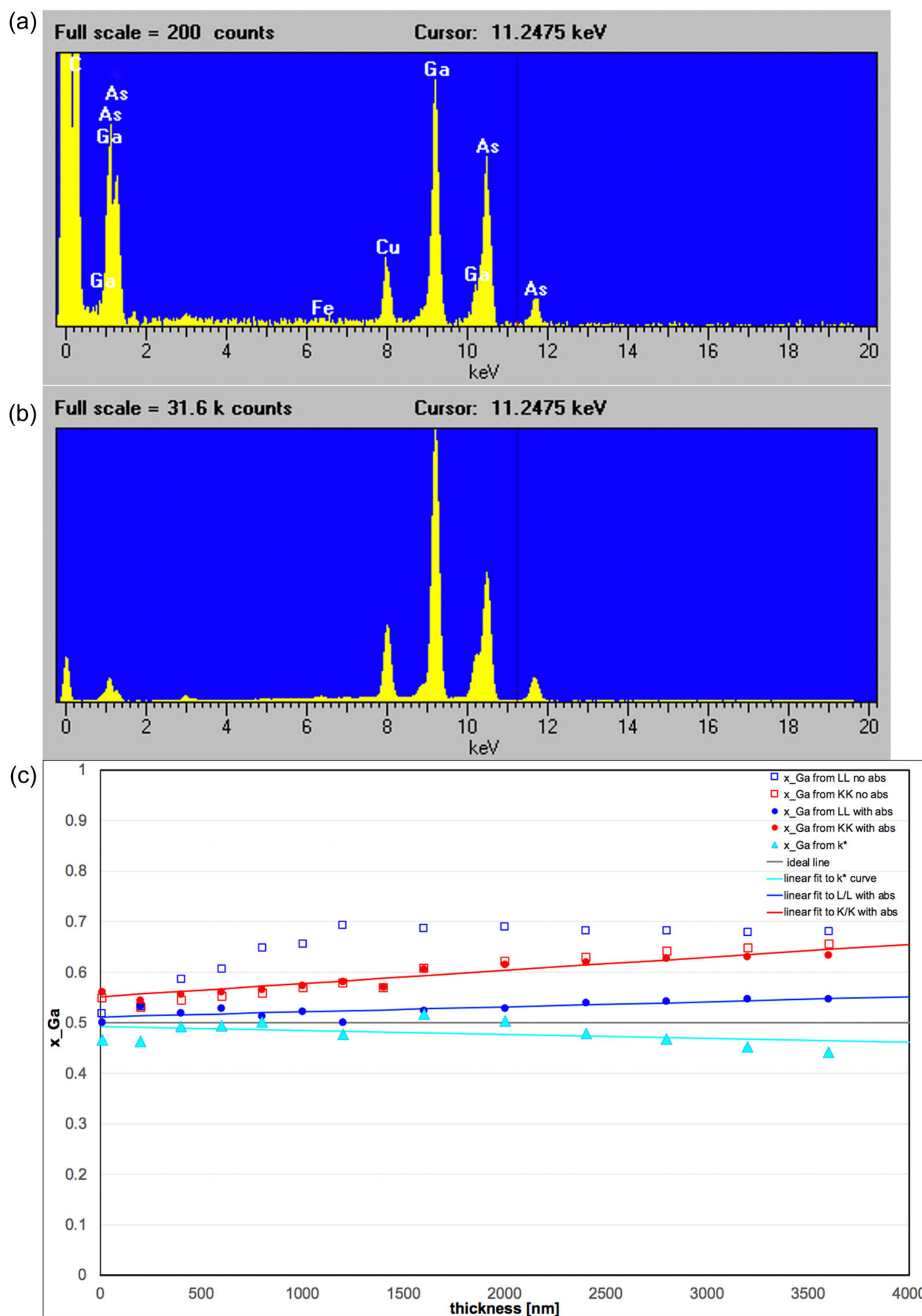

FIGURE 10 X-ray spectra at 200 kV from pure GaAs cleaved wedges at thicknesses of (a) 200 nm and (b) 3200 nm. (c) Plot of the apparent gallium content, x_{Ga}, as a function of thickness for different line types analysed and different methods of absorption correction (ZAF vs. k^*).

27024288, 0, Downloaded from https://onlinelibrary.wiley.com/doi/10.1002/appl.202300128 by University Of Sheffield, Wiley Online Library on [06/08/2024]. See the Terms and Conditions (https://onlinelibrary.wiley.com/terms-and-conditions) on Wiley Online Library for rules of use; OA articles are governed by the applicable Creative Commons License

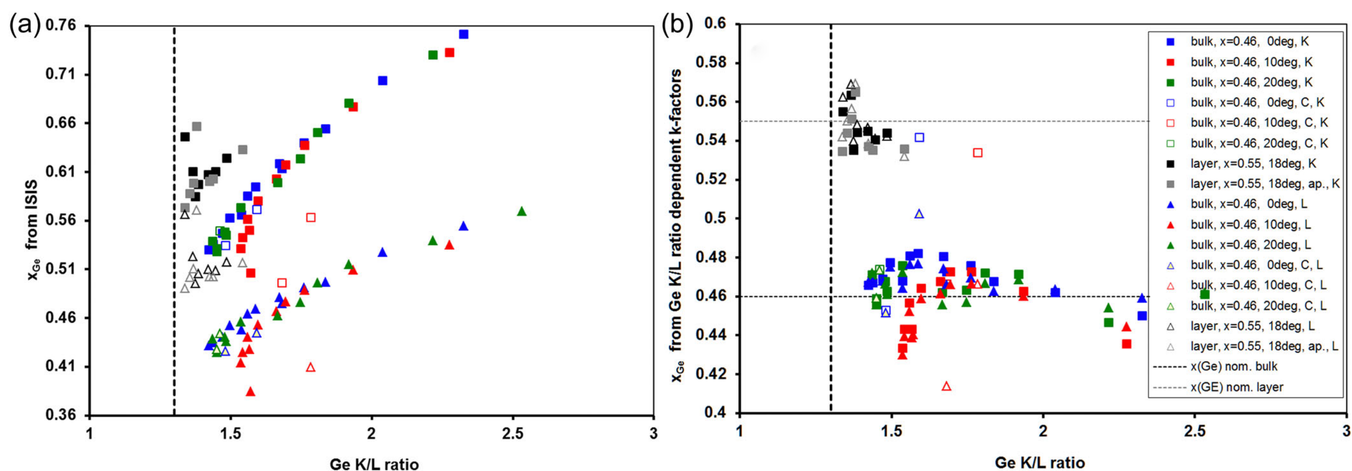

FIGURE 11 Analysis of the apparent germanium content, xGe, of two different Si1–xGex samples. Colour: bulk Si0.54Ge0.46, black and white: $Si_{0.45}Ge_{0.55}$ strained thin film sample. (a) Direct ZAF output from Oxford Instruments ISIS software, (b) k^*-factor method. Vertical lines delineate the lowest Ge K/L ratio of 1.3 predicted by CASINO simulations of SiGe, horizontal lines indicate the nominal compositions of both samples. The degree values and letters C, K and L in the legend to the right common to both plots refer to sample tilt angle, visible carbon contamination, Ge K-line or L-line used for quantification. *Source*: Adapted from Qiu et al. [4].

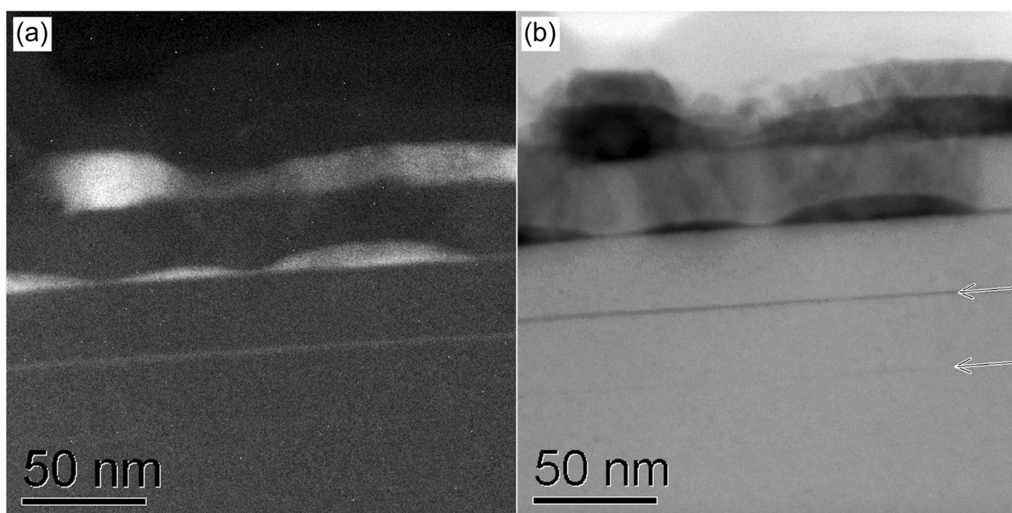

FIGURE 12 Annular dark field (a) and bright field (b) scanning transmission electron microscope images of Ge/Si(001).

indium enrichment within the quantum dot cores compared to their surrounding wetting layer but also a substantial indium depletion in the wetting layer just around the quantum dots, visible as a dark halo around some quantum dots in Figure 8a,c. This has been the key to understanding the Stranski–Krastanow growth in InGaAs [26] that describes the spontaneous transition from two-dimensional flat layer to three-dimensional island growth and enables self-organised quantum dot epitaxy.

Figure 9 demonstrates the high sensitivity of STEM-EDX. The top and bottom show 2.4 nm GaAs/2.0 nm $Al_xGa_{1-x}As$ superlattices whose measured Al-content of $x = 0.18$ lies below the nominal value of $x_{nom} = 0.33$, in agreement with beam broadening by an effective probe just slightly wider than 1 nm (rms width). This is sufficient to pick up, slightly above the centres of the maps, a tiny signal from the Al K-line between an InGaAs quantum dot layer deposited on top an InGaAs quantum well where the aluminium effusion cell had been briefly opened, depositing the equivalent of nominal 0.3 monolayers of a full group III lattice plane, corresponding to a single monolayer of $Al_{0.3}In_{0.35}Ga_{0.35}N$ within the $In_{0.5}Ga_{0.5}N$ quantum dot layer.

Figure 10 demonstrates the problem of absorption correction in thin and thick samples, in this case of GaAs, which would be needed for full STEM-EDX quantification. The apparent gallium content of pure GaAs wedge samples varies with the type of X-ray lines chosen for quantification (K vs. L), the type of absorption correction applied (none vs. ZAF vs. k^*, or indeed any other) and can depend heavily on sample thickness, t. The answer for the apparent Ga content of

27024288, 0, Downloaded from https://onlinelibrary.wiley.com/doi/10.1002/appl.202300128 by University Of Sheffield, Wiley Online Library on [06/08/2024]. See the Terms and Conditions (https://onlinelibrary.wiley.com/terms-and-conditions) on Wiley Online Library for rules of use; OA articles are governed by the applicable Creative Commons License

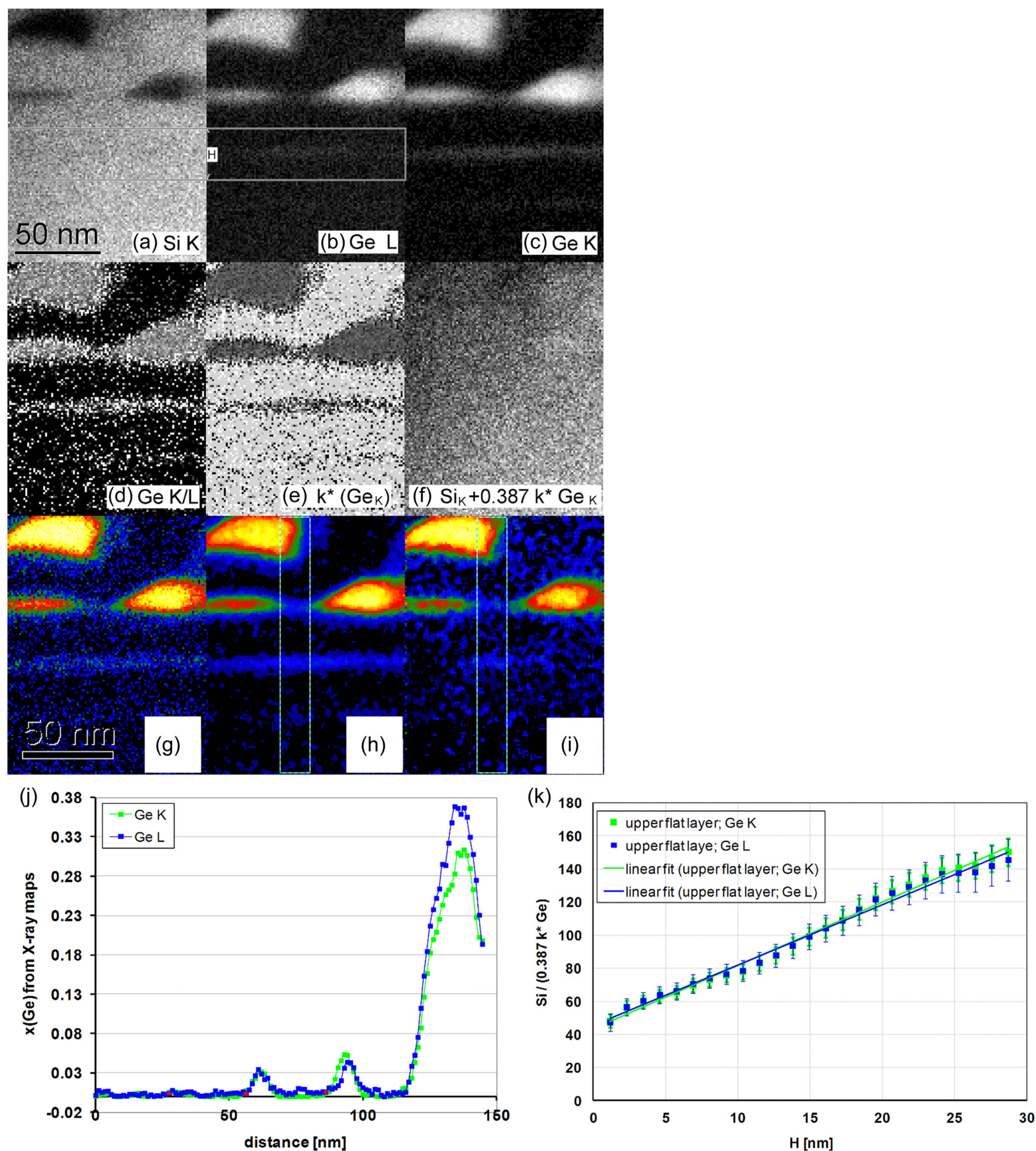

FIGURE 13 Raw X-ray maps (a)–(c), map of Ge K/L ratio (d), map of $k^*_{\mathrm{GeK,SiK}}$ (e) and of the sum signal of $\mathrm{Si_K}$ and 0.387 $k^* \times \mathrm{Ge_K}$ which is essentially featureless (f). The factor 0.387 is the ratio of the atomic weights of Si to Ge atoms so that results are in at % rather than weight %. (g)–(i) False-colour maps of the Ge content in the SiGe layers and islands from raw $\mathrm{Ge_K}$ (g), smoothed $\mathrm{Ge_K}$ (h) and $\mathrm{Ge_L}$ (i). The latter two were used to extract line profiles (j) of x_{Ge} along the vertical growth direction between the islands to determine the maximum Ge content of SiGe layers as $x \approx 0.3$ before they start to roughen. (k) is a plot of the Si/Ge atomic ratio integrated along the layers over a window of height H, as indicated in (b), the inverse of which directly gives the total Ge content in this upper flat layer as 1.85 ± 0.21 ML. *Source*: Adapted from Norris et al. [29].

27024288, 0, Downloaded from https://onlinelibrary.wiley.com/doi/10.1002/appl.202300128 by University Of Sheffield, Wiley Online Library on [06/08/2024]. See the Terms and Conditions (https://onlinelibrary.wiley.com/terms-and-conditions) on Wiley Online Library for rules of use; OA articles are governed by the applicable Creative Commons License

stoichiometric GaAs treated as a Ga_xAs_{1-x} alloy from quantification of K-lines (Ga_K/As_K ratio) using ZAF (red dots) gives $x_{Ga,\ KK} = (55.1 + 2.6 \times t/\mu m)$ at% so is both too large and still contains a lot of thickness dependence. The answer from L-line quantification (Ga_L/As_L ratio) using ZAF (blue dots) gives $x_{Ga,LL} = (51.1 + 1.0 \times t/\mu m)$, which is better but still >50 at%. Using the k^*-factor approach (cyan triangles) gives $x_{Ga^*} = (49.18 - 0.76 \times t/\mu m)$ at%, which is much closer to the correct value of $x = 50$ at% although the overall scatter over all data points is still a bit large, and simple averaging of all would give a mean of 48.0 ± 2.2 at% [28].

In Figure 11, we compare STEM-EDX quantification for two SiGe samples for the standard, ZAF-based absorption correction (a) and the k^*-factor method (b). With standard ZAF quantification (a) the spread is large, results from K- and L-line quantification are inconsistent and there is still a strong thickness dependence, indicating the estimated thickness and/or the absorption correction model has been wrong. With k^*-factor correction (b) the exact same data sets are producing much more consistent answers (K- and L-line quantification now agree to within 0.3 at%) and the clouds of data points are much smaller, with rms spreads corresponding to ±1.2 at%, so $Si_{0.54}Ge_{0.46}$ and $Si_{0.45}Ge_{0.55}$ can now be distinguished with total confidence for all thicknesses.

The k^*-factor method of absorption correction relies on the K/L ratio of X-ray lines of a specific element (such as Ga or As in InGaAs, or of Ge in SiGe) serving as an in-built reference for how strong absorption is so it works for every spectrum with at least one heavy element with multiple X-ray lines. Monte Carlo simulations have shown for these semiconductors that up to 2 µm specimen thickness the K/L ratios of As, Ga or Ge, respectively, increase monotonically, almost linearly, with specimen thickness [6] so can be used as a proxy thereof. The reason for this is that thicker samples mean that softer L-lines of X-rays will be more strongly absorbed than harder K-line X-rays from the same element. The practical advantage is that, firstly, while real specimen thicknesses are always prone to measurement errors, K/L ratios can be extracted from every spectrum straight away without much error and, secondly, specimen geometries other than thin plan-parallel slabs will influence X-ray absorption and this will directly be reflected in changes of K/L intensity ratios even if the local thickness remains unchanged.

This approach has been extended from X-ray spectra to maps. Figure 12 shows STEM images of Ge layers grown at 400°C for different thicknesses below and above the Stranski–Krastanow transition on Si(001). The arrows point to two flat layers that essentially are SiGe alloy layers due to segregation and interdiffusion; if the layer thicknesses deposited increase further then first islands form on the wetting layer before eventually a loss of epitaxy and crystallinity occurs.

As shown in Figure 13, the raw X-ray maps in the top row can be further processed for quantification, enabling us to extract quantitative compositional profiles from which we could calculate the maximum thickness and Ge content of flat SiGe layers before they transition to island growth [29], very similar to compressively strained In(Ga)As layers.

SUMMARY AND CONCLUSION

It has been shown how X-ray spectra and maps can be quantified beyond what is currently available from textbooks. This includes

(a) for SEM-EDX:

- determining in top-down geometry the thickness of thin surface layers that contain at least one element that is not present in the underlying substrate, down to sub-nm accuracy, which is similar to what typical surface science measurements can achieve;
- measuring in cross-sectional geometry the total amount of a certain material deposited as a thin film or segregated to the surface by integrating the compositional profiles where the resulting sensitivity and accuracy can be far below the electron beam size;

(b) for STEM-EDX:

- quantifying self-consistently the chemical composition of material in electron transparent samples for (S)TEM if they contain at least one heavy element with a detectable K-line and an L-line, based on the self-consistent absorption correction using k^*-factors;
- an extension of the k^*-factor method from single spectra to multiple spectra maps that perform the absorption correction point-by-point using the local K/L ratios measured at every point. This can be used to extract fully quantitative compositional profiles from maps along arbitrary directions.

ACKNOWLEDGEMENTS

The author acknowledges Mark Hopkinson (University of Sheffield) and Emil-Mihai Pavelescu (National Institute for R&D in Microtechnologies, Bucharest) for provision of InGaAs samples. The SiGe bulk sample was kindly provided by Ichiro Yonenaga, Tohoku University, Sendai. The SiGe thin film sample was grown by Maksym Myronov at the University of Warwick, Coventry. Previous colleagues Yang Qiu and David J. Norris (for SiGe) and Meilyr C. Parri (for InGaAs) are acknowledged for help with experimental electron microscopy and data analysis.

CONFLICT OF INTEREST STATEMENT

The authors declare no conflict of interest.

DATA AVAILABILITY STATEMENT

The data that support the findings of this study are available from the corresponding author upon reasonable request.

ORCID

Thomas Walther http://orcid.org/0000-0003-3571-6263

REFERENCES

[1] L. Reimer, *Scanning Electron Microscopy—Physics of Image Formation and Microanalysis*, 2nd ed., Springer, Berlin **1998**.

27024288, 0, Downloaded from https://onlinelibrary.wiley.com/doi/10.1002/appl.202300128 by University Of Sheffield, Wiley Online Library on [06/08/2024]. See the Terms and Conditions (https://onlinelibrary.wiley.com/terms-and-conditions) on Wiley Online Library for rules of use; OA articles are governed by the applicable Creative Commons License

[2] J. I. Goldstein, D. E. Newbury, P. Echlin, D. C. Joy, C. E. Lyman, E. Lifshin, L. Sawyer, J. R. Michael, *Scanning Electron Microscopy and X-ray Microanalysis*, 3rd ed., Springer, New York **2003**.

[3] D. B. Williams, C. B. Carter, *Transmission Electron Microscopy: A Textbook for Materials Science*, 2nd ed., Springer, New York **2009**.

[4] Y. Qiu, V. H. Nguyen, A. Dobbie, M. Myronov, T. Walther, *J. Phys. Conf. Ser*. **2013**, *471*, 012031.

[5] T. Walther, X. Wang, *J. Phys. Conf. Ser*. **2015**, *644*, 012006.

[6] M. C. Parri, Y. Qiu, T. Walther, *J. Microsc*. **2015**, *260*(3), 427.

[7] E. J. Kirkland, *Advanced Computing in Electron Microscopy*, 3rd ed., Springer, Cham **2020**.

[8] D. Drouin, A. R. Couture, D. Joly, X. Tastet, V. Aimez, R. Gauvin, *Scanning* **2007**, *29*, 92.

[9] T. Walther, *Nanomaterials* **2022**, *12*(13), 2220.

[10] T. Walther, *Nanomaterials* **2021**, *11*(8), 2117.

[11] H. Demers, N. Brodusch, R. Gauvin, *Microsc. Microanal*. **2017**, *23*(S1), 1044.

[12] J. L. Pouchou, F. Pichoir, *Scanning* **1990**, *12*, 212.

[13] Y. Yuan, H. Demers, S. Rudinsky, R. Gauvin, *Microsc. Microanal*. **2019**, *25*, 92.

[14] A. J. D'Alfonso, B. Freitag, D. Klenov, L. J. Allen, *Phys. Rev. B Condens. Matter Mater. Phys*. **2010**, *81*, 100101R.

[15] H. S. von Harrach, P. Dona, B. Freitag, H. Soltau, A. Niculae, M. Rohde, *J. Phys. Conf. Ser*. **2010**, *241*, 012015.

[16] B. D. Forbes, A. J. D'Alfonso, R. Williams, R. Srinivasan, H. L. Fraser, D. W. McComb, B. Freitag, D. O. Klenov, L. J. Allen, *Phys. Rev. B Condens. Matter Mater. Phys*. **2012**, *86*(2), 024108.

[17] X. Wang, J. Bai, T. Walther, *J. Microsc*. **2018**, *272*(2), 111.

[18] T. Walther, *J. Phys. Conf. Ser*. **2010**, *209*, 012029.

[19] G. Cliff, G. W. Lorimer, *J. Microsc*. **1975**, *103*, 203.

[20] R. Tixier, J. Philibert, in *Vth International Congress on X-Ray Optics and Microanalysis* (Eds: G. Möllenstedt, K. H. Gaukler), Springer, Berlin, **1969**, p. 180.

[21] M. Watanabe, D. B. Williams, *J. Microsc*. **2006**, *221*(2), 89.

[22] O. Eibl, *Ultramicroscopy* **1993**, *50*(2), 179.

[23] M. Watanabe, Z. Horita, M. Nemoto, *Ultramicroscopy* **1996**, *65*(3–4), 187.

[24] T. Walther, X. Wang, *J. Microsc*. **2016**, *262*(2), 151.

[25] S. L. Liew, T. Walther, S. Irsen, M. Hopkinson, M. S. Skolnick, A. G. Cullis, *Springer Procs. Phys*. **2007**, *120*, 259.

[26] T. Walther, A. G. Cullis, D. J. Norris, M. Hopkinson, *Phys. Rev. Lett*. **2001**, *86*(11), 2381.

[27] T. Walther, J. Nutter, J. P. Reithmaier, E. M. Pavelescu, *Semicond. Sci. Technol*. **2020**, *35*, 084001.

[28] T. Walther, *J. Phys. Conf. Ser*. **2010**, *241*, 012016.

[29] D. J. Norris, Y. Qiu, A. Dobbie, M. Myronov, T. Walther, *J. Appl. Phys*. **2014**, *115*, 012003.

How to cite this article: T. Walther, *Appl. Res*. **2024**, e202300128. https://doi.org/10.1002/appl.202300128

27024288, 0, Downloaded from https://onlinelibrary.wiley.com/doi/10.1002/appl.202300128 by University Of Sheffield, Wiley Online Library on [06/08/2024]. See the Terms and Conditions (https://onlinelibrary.wiley.com/terms-and-conditions) on Wiley Online Library for rules of use; OA articles are governed by the applicable Creative Commons License